Enhanced Oxygen Ion Conductivity and Mechanistic Understanding in $Ba_3Nb_{1-x}V_xMoO_{8.5}$

Sacha Fop,*,† Kirstie McCombie,† Ronald I. Smith‡ and Abbie C. Mclaughlin *,†

† Department of Chemistry, University of Aberdeen, Meston Walk, Aberdeen AB24 3UE, United Kingdom.

‡ ISIS Facility, Rutherford Appleton Laboratory, Harwell, Didcot OX11 0DE, United Kingdom.

ABSTRACT: Significant oxide ion conductivity has recently been reported in the cation-deficient hexagonal perovskite derivative $Ba_3NbMoO_{8.5}$. This system exhibits considerable anion and cation disorder. Oxygen disorder enables the ionic conduction and is generated by the competitive occupation of two available average tetrahedral/octahedral oxygen positions within the palmierite-like layers of the average crystal structure. A random distribution of cationic vacancies leads to the formation of complex disordered stacking configurations of the constituting polyhedral units. Here, we report on the electrical and structural properties of the series $Ba_3Nb_{1-x}V_xMoO_{8.5}$ (x = 0.0, 0.1, 0.2, 0.3, 0.4). Neutron diffraction data evidence that substitution of Nb^{5+} by V^{5+} leads to an increase in the average concentration of lower coordination $M1O_x$ units, which is also accompanied by an increase in polyhedral distortion. Bond-valence site energy (BVSE) calculations on the average structure reveal that the ionic migration along the palmierite-like layers is comprised by two energy barriers relative to the populations of the average oxygen crystallographic sites and to the distortion of the flexible $M1O_x$ units. The compound with x = 0.1, $Ba_3Nb_{0.9}V_{0.1}MoO_{8.5}$, shows the lowest activation energy, and high bulk ionic conductivity: ~ 0.01 S cm^{-1} at 600 °C, almost one order of magnitude higher than the bulk conductivity of the parent compound. $Ba_3Nb_{0.9}V_{0.1}MoO_{8.5}$ presents predominant ionic conductivity and good stability in a wide oxygen partial pressure range, making it a promising candidate for solid electrolyte applications.

Introduction

Oxide ion conductors are an important class of materials, with application in various energy-related technologies, such as solid oxide fuel cells (SOFCs) and solid oxide electrolysis cells (SOECs). [1, 2] One current drawback of SOFCs and SOECs is the high working temperatures (> 700 °C) necessary for the ionic transport through commercially available solid electrolytes in order to enable the electrochemical reactions at the electrode interfaces. The high operating temperature results in high costs, poor durability and material compatibility challenges. [1, 3] Research into the development of electrolyte materials possessing good ionic conduction at intermediate temperatures (300 – 600 °C) has led to the discovery of oxide ion conductivity in various structural families. [1, 4, 5, 6, 7, 8, 9, 10, 11, 12, 13, 14] The oxide ion conduction in these materials is mediated by oxygen vacancies or interstitials. [7, 8, 11, 13] A disordered oxygen sub-lattice often accommodates the defects necessary for the ionic diffusion, which is generally assisted by a flexible cationic sub-lattice. [5, 12, 14, 15]

Recently, we have reported significant oxide ion conductivity in the hexagonal cation-deficient perovskite derivative $Ba_3NbMoO_{8.5}$. [16] $Ba_3NbMoO_{8.5}$ presents a bulk conductivity of 2.2 x 10^{-3} S cm^{-1} at 600 °C, comparable with other solid electrolyte materials. The conductivity is predominantly ionic in a wide pO_2 range from 10^{-20} to 1 atm. $Ba_3NbMoO_{8.5}$ has an average structure composed by a hybrid of the 9R perovskite and palmierite units. [16] The 9R perovskite ($A_3B_3O_9$) is composed by trimers of face sharing octahedral units connected by corner sharing, with stacking sequence $(hhc)_3$ (Figure 1a). [17] The palmierite ($A_3B_2O_8$) structure is a cation-deficient derivative of the 9R perovskite, in which the cubic [BaO_3] layers are replaced by oxygen-deficient [BaO_2] layers, thus resulting in the formation of isolated tetrahedral units spaced by empty octahedral sites (Figure 1b). [17] In the average hybrid model of $Ba_3NbMoO_{8.5}$, the cation vacancies are distributed on two partially occupied metal sites (M1 and M2), forming hybrid trimer stacks. Considerable positional oxygen disorder, which originates from partial occupation of two average oxygen positions (O2 and O3) within the palmierite-like layers (of average composition [$BaO_{2.5}$]) leads to the formation of polyhedral units ($M1O_x$) with variable coordination (Figure 1c). [16, 18] A pair distribution function study has indeed demonstrated the existence of local 4-, 5-, and 6-fold M1 geometries. [19] The random distribution of intrinsic oxygen vacancies and available oxygen sites produces a continuous 2-dimensional diffusion pathway, enabling the oxide ions migration along the palmierite-like layers. [20]

A variable temperature neutron diffraction study of $Ba_3NbMoO_{8.5}$ has revealed a thermal rearrangement in the relative average occupancy of the O2/O3 sites. [21] Redistribution of the oxygen population in favor of the average tetrahedral O3 position above 300 °C denotes the preference of the M1 cations for lower coordination environments as the temperature rises. Results from PDF analysis equally evidenced an increase in the number of local tetrahedral $M1O_4$ units at high temperature, at the expenses of the number of

MO_6 octahedra, although the 5-fold coordination appears to be prevalent on the local scale. [19] The relative occupation of the average O2/O3 sites is also affected by the nature of the M cations. $Ba_3NbMo_{1-x}M_xO_{8.5}$ compositions where Mo^{6+} is substituted by M = Nb^{5+} or W^{6+}, two cations which generally prefer higher coordination environments, [22] exhibit higher occupancy of the average octahedral O2 position. [23, 24, 25, 26, 27] There is a strong relationship between the ionic conductivity and the average distribution of the oxide ions on the O2/O3 sites. Higher O3 occupancy, and higher concentration of average lower coordination environments, are linked with an increase in the dynamic mobility (and hence in the conductivity) of the oxide ions. [21] This is corroborated by the fact that Nb- and W-doped systems with prevalence of higher coordination geometries (MO_6), due to larger occupation of the average O2 site, show reduced conductivity. [23, 24, 25, 26, 27] We have previously predicted that introduction of dopant cations known to preferentially support lower coordination environments would enhance the conductivity. [28]

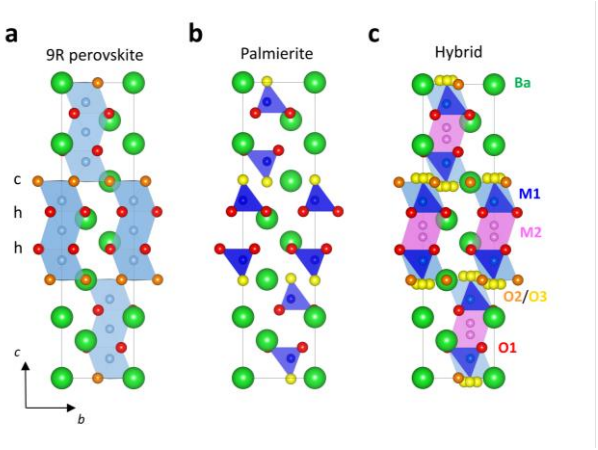

Figure 1. (a) 9R perovskite and (b) palmierite structures. (c) Average hybrid crystal structure of $Ba_3NbMoO_{8.5}$. Blue and light blue polyhedra represent the average MO_x units created by partial occupation of O2 and O3. In the hybrid model, the M2 and O3 positions are split from the ideal sites to account for the cation and anion disorder.

Here we report the structural and electrical properties of the series $Ba_3Nb_{1-x}V_xMoO_{8.5}$ (x = 0.0, 0.1, 0.2, 0.3, 0.4). Nb^{5+} is replaced by V^{5+}, which is a cation with a strong preference for 4-fold coordination geometry. [22] This substitution effectively leads to an increase in the occupation of the O3 crystallographic site. The V-doped compositions have generally higher total conductivity values than the parent compound. Notably, the composition with x = 0.1 exhibits a bulk ionic conductivity of ~ 0.01 S cm^{-1} at 600 °C, almost one order of magnitude higher than the bulk conductivity of $Ba_3NbMoO_{8.5}$. Importantly, $Ba_3Nb_{0.9}V_{0.1}MoO_{8.5}$ presents predominant ionic conductivity in a wide oxygen partial pressure range and good stability under reducing conditions, making it an attractive candidate for electrolyte applications. Bond-valence site energy (BVSE) analysis on the average structure demonstrates the presence of two relative energy barriers for the oxide ion migration within the palmierite-like layers. The conduction activation energy is the sum of the interplay between the relative distribution of average coordination geometries and the average distortion of the polyhedral units.

Experimental section

$Ba_3Nb_{1-x}V_xMoO_{8.5}$ (x = 0.0, 0.1, 0.2, 0.3, 0.4) compounds were prepared by the solid-state reaction method. Mixtures of stoichiometric amounts of $BaCO_3$ (99.999% Aldrich), Nb_2O_5 (99.99% Aldrich), V_2O_5 (99.95%, Aldrich) and MoO_3 (99.5+%, Aldrich) were ground, pelleted, and calcined at 900 °C for 10 hours. The pellets were subsequently ground and heated at 1100 °C for 48 hours. The heating step was repeated until phase pure products were obtained.

Laboratory X-ray powder diffraction (XRD) patterns were collected on a PANalytical Empyrean diffractometer equipped with a Cu Kα tube and a Johansson monochromator. Data were recorded in the range 10° < 2θ < 120°, with a step size of 0.013°.

Thermogravimetric analysis (TGA) was performed with a Mettler Toledo TGA 2 coupled with a Hiden Quadrupole Mass Spectrometer (MS) in dry air and 5% H_2 (in N_2) atmospheres, with a heating rate of 10 °C/min. Scanning electron microscopy (SEM) images were collected using a field emission gun Carl Zeiss Gemini SEM 300 with an XMax 80 detector and an AZtecHKL EBSD analysis system with a Nordlys Nano EBSD camera (Oxford Instruments Ltd.).

The electrical properties of the $Ba_3Nb_{1-x}V_xMoO_{8.5}$ (x = 0.0, 0.1, 0.2, 0.3, 0.4) series were measured by AC impedance spectroscopy, with a Solartron 1260 impedance analyzer in the frequency range 0.1 Hz – 1 MHz with an applied alternating voltage of 0.1 V. Measurements were performed on platinum coated dense pellets (> 95% of the theoretical neutron diffraction density) of approximately ~ 1 mm thickness and ~10 mm diameter, upon cooling from 600 °C in a sealed tube furnace and allowing 2 hours of equilibration at each temperature step. Dry gaseous atmospheres, obtained by flowing the employed gas through a column of a commercial desiccant (Drierite) (pH_2O < 10^{-4} atm), were employed for the measurements in air, O_2, N_2 and 5% H_2 (in N_2). For the measurements in humidified air, the gas was bubbled through a water-filled Dreschel bottle at ambient temperature (pH_2O ~ 0.021 atm). The reliability of the measured impedance data was evaluated using Kramers-Kronig (KK) transformations. Kramers-Kronig validation ensures that the impedance response is a representation of a linear, time-invariant (i.e. at equilibrium) and casual system. [29] The *Lin-KK* tool software was employed to perform KK tests on the collected impedance data. [30] Typical KK residual plots for the measurements in dry air at selected temperatures are reported in Supporting Figure S5.

Time-of-flight (TOF) neutron diffraction experiments were performed on the POLARIS diffractometer at ISIS (Rutherford Appleton Laboratory, Harwell, Oxford, UK) at ambient temperature (25 °C). Data were acquired on samples of 5 g of $Ba_3Nb_{1-x}V_xMoO_{8.5}$ (x = 0.0, 0.1, 0.2, 0.3, 0.4). The samples were loaded into an 8 mm vanadium can and data were acquired using all four detector banks with a total scan time of 2 hours. Rietveld analysis was performed using the GSAS/EXPGUI package. [31] The neutron diffraction datasets were used in combination with high-resolution laboratory X-ray diffraction data (scan time of 16 hours) for the refinement of the crystal structure. Vanadium has a small neutron

scattering length and is practically invisible to neutrons. [32] Using neutron data in combination with X-ray diffraction data allows more accurate information, especially regarding the metal fractional occupancies, to be obtained. The background was fitted by the Chebyschev polynomial function and the peak shapes were modelled using a pseudo-Voigt function.

Bond-valence site energy (BVSE) calculations were performed with the *soft*BV program. [33, 34] *Soft*BV is a computationally inexpensive software tool which utilizes a force-field algorithm based on the bond-valence sum (BVS) approach for the computation of possible migration pathways and relative migration barriers in ionically conducting materials. *Soft*BV analyzes the entire energy landscape, providing information on the connecting local minima and saddle points (identified by fractional coordinate values) and the relative energy barriers for each pathway segment. The *soft*BV force-field is constituted by a BVS Morse-type term describing the attractive interaction and short-range Born-repulsion between cation-anion pairs, and by a Coulomb term for the cation-cation and anion-anion repulsion interactions. [33] While BVS conventionally only considers first coordination shell interactions, the Morse-type potential in *soft*BV includes bond-softness sensitive bond-valence parameters which take into account contributions from higher coordination shells, thus yielding more sensible results in the calculation of valence sums for mobile ions. [33, 34, 35] Using the structural models from Rietveld refinement as input, bond-valence site energy landscapes for the interaction of a test O^{2-} ion were calculated for a dense grid of points with a resolution of 0.1 Å. Diffusion pathways were identified with regions of low bond-valence site energy by direct visualization of the connectivity of the isosurfaces and by examination of the calculated pathway segments. BVSE models of migration barriers were plotted from the calculated energy profiles of the pathway segments.

Analysis of minimum bonding ellipsoids using the PIEFACE software was employed to evaluate the effect of doping on the relaxation of the average metal coordination polyhedra. [36] Polyhedral distortion was quantified by the standard deviation, $\sigma(R)$, of the three principal ellipsoids's radii (R_x, R_y, R_z).

Results and discussion

Laboratory X-ray diffraction (XRD) confirmed all the as prepared $Ba_3Nb_{1-x}V_xMoO_{8.5}$ (x = 0.0, 0.1, 0.2, 0.3, 0.4) samples to be phase pure (Supporting Figure S1). All the patterns could be indexed with the space group $R\bar{3}m$ *H*, in agreement with previous reports. [16] SEM micrographs were collected on dense $Ba_3Nb_{1-x}V_xMoO_{8.5}$ pellets. Secondary electron (SE) images show grains ranging in size between ~ 20 – 50 μm; no secondary phases were observed in the backscattering (BSE) images of the surface and section of the pellets (Supporting Figure S2).

The electrical properties of the $Ba_3Nb_{1-x}V_xMoO_{8.5}$ (x = 0.0, 0.1, 0.2, 0.3, 0.4) series were measured by AC impedance spectroscopy. Typical complex impedance plane (Z^*) plots for the parent (x = 0.0) composition are composed by two arcs at high and intermediate frequencies, representing the bulk (capacitance values ~ 4.0 – 6.5 pF cm^{-1}) and grain boundary (~ 0.20 – 0.30 nF cm^{-1}) responses respectively (Supporting Figure S3). As the temperature increases, a low-slope electrode Warburg response indicative of ionic diffusion is observed at low frequencies (Supporting Figure S3b). [37] The impedance spectra are like those previously reported for $Ba_3NbMoO_{8.5}$. [16] The complex impedance plots of the V-doped compositions (x = 0.1, 0.2, 0.3, 0.4) are depressed and show poor resolution between the bulk (~ 7.7 – 10.2 pF cm^{-1}) and grain boundary (~ 0.07 – 0.2 nF cm^{-1}) responses (Supporting Figure S4). A pronounced Warburg signal inclined at ~ 45° is seen for all compositions. At higher temperatures, another feature appears between the grain arc and the electrode signal; this feature shows capacitance value of ~1 – 2 μF cm^{-1} and is associated with charge transfer to and from the oxide ions at the electrode-ceramic interface. [37] The total resistivity values (R_b + R_{gb}) for all the compositions were extracted from the high frequency intercept of the grain boundary arc. The total conductivity values are presented in the Arrhenius plot in Supporting Figure S6. The V-doped compositions with x = 0.1, 0.2, 0.3 show increased total conductivity values, compared to the parent compound. The composition with x = 0.1 exhibits the highest total conductivity; at 600 °C, the total conductivity of $Ba_3Nb_{0.9}V_{0.1}MoO_{8.5}$ is 3.8 x 10^{-3} S cm^{-1}, one order of magnitude higher than the value for $Ba_3NbMoO_{8.5}$, which has a total conductivity of 3.4 x 10^{-4} S cm^{-1}. Equivalent circuit analysis was performed to extract the bulk conductivity values; a detailed description of the analysis can be found in the Supporting Information. A representative equivalent circuit fit of the complex impedance data of $Ba_3Nb_{0.9}V_{0.1}MoO_{8.5}$ is shown in Figure 2a, b and Supporting Figure S8b. The good quality of the fit is revealed by the match between the observed and calculated spectra and by inspection of the distribution of residuals against the frequency (Supporting Figure S9). Typical fitting parameters are reported in Supporting Table S1. The Arrhenius plot in Figure 2c evidences a significant increase in the bulk conductivity value for x = 0.1 in comparison with the parent composition. $Ba_3Nb_{0.9}V_{0.1}MoO_{8.5}$ presents a bulk conductivity of 1.01 x 10^{-2} S cm^{-1} at 600 °C while the bulk conductivity of $Ba_3NbMoO_{8.5}$ is 2.0 x 10^{-3} S cm^{-1} at the same temperature, an increase of nearly one order of magnitude. Similar to the parent composition, the conductivity of $Ba_3Nb_{0.9}V_{0.1}MoO_{8.5}$ shows a change in slope above 500 °C, with the activation energy reducing from 1.17 (4) eV to 0.51 (1) eV, which is substantially lower than the activation energy of $Ba_3NbMoO_{8.5}$ (0.73 (1) eV). The Arrhenius plot of the bulk ionic conductivity of all $Ba_3Nb_{1-x}V_xMoO_{8.5}$ phases is displayed in Figure S10 showing that $Ba_3Nb_{0.9}V_{0.1}MoO_{8.5}$ presents the highest bulk conductivity.

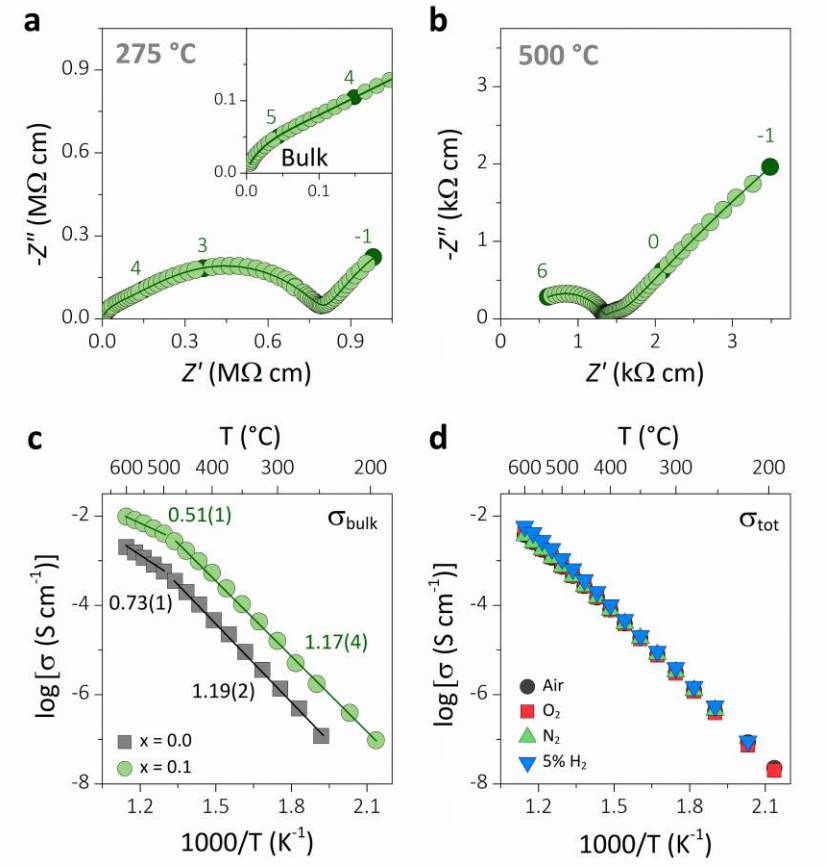

Figure 2. Impedance spectroscopy and conductivity of $Ba_3Nb_{0.9}V_{0.1}MoO_{8.5}$. Complex impedance plots of $Ba_3Nb_{0.9}V_{0.1}MoO_{8.5}$ recorded under dry air at 275 °C (a) and 500 °C (b). The numbers and corresponding filled circles indicate selected frequency decades; the dark green line is the equivalent circuit fitting. (c) Arrhenius plot of the bulk ionic conductivity of $Ba_3Nb_{0.9}V_{0.1}MoO_{8.5}$ (x = 0.1) compared with the bulk conductivity of the parent compound (x = 0.0); activation energies are reported in eV. (d) Total conductivity of $Ba_3Nb_{0.9}V_{0.1}MoO_{8.5}$ recorded under a range of different atmospheres showing a negligible electronic component.

Impedance spectroscopy measurements on $Ba_3Nb_{0.9}V_{0.1}MoO_{8.5}$ were also performed in a range of different atmospheres. Measurements carried out in air, O_2 and N_2 evidence that the total conductivity is independent of oxygen partial pressure at high and intermediate pO_2 values (see the Arrhenius plot in Figure 2d and Supporting Figure S11a), a behavior consistent with pure oxygen ion diffusion. There is a very slight increase in the total conductivity at high temperatures under the most reducing atmosphere (5% H_2 (in N_2)), suggesting a small electronic component to the conductivity. Concentration cell experiments in air/5% H_2 have already revealed a minor electronic component in $Ba_3NbMoO_{8.5}$ under similar conditions (ionic transport number of 0.90 – 0.94). [16] However, the presence of clear Warburg/electrode responses at all temperatures in the complex impedance plots recorded in reducing 5% H_2 (in N_2) (Supporting Figure S11b) indicates that the electronic component in $Ba_3Nb_{0.9}V_{0.1}MoO_{8.5}$ is small and the conductivity is predominantly ionic. [38] Additional impedance spectroscopy measurements performed under humidified air atmosphere (pH_2O ~ 0.021 atm) do not evidence any significant increase in the total conductivity of $Ba_3Nb_{0.9}V_{0.1}MoO_{8.5}$ (and of any of the members of the V-doped series), implying that there is no proton conduction in this material (Supporting Figure S12). We have recently reported significant protonic conductivity in the hexagonal perovskite derivative $Ba_7Nb_4MoO_{20}$, with an average structure composed by a disordered arrangement of 12R hexagonal perovskite and palmierite-like layers, analogously to $Ba_3NbMoO_{8.5}$. [39] In this material, proton conduction along the palmierite-like layers is enabled by the presence of a predominant tetrahedral environment; on the other hand, $Ba_3NbMoO_{8.5}$ does not show any proton conductivity which is thought to be due to the larger number of higher coordination geometries. [16, 19] V-doped $Ba_3NbMoO_{8.5}$ materials present a higher relative number of lower coordination polyhedral units than the parent compound (as described below), but there is no evidence of a protonic contribution to the conductivity. Overall, the impedance spectroscopy measurements demonstrate that $Ba_3Nb_{0.9}V_{0.1}MoO_{8.5}$ exhibits predominant oxide ionic conductivity.

The stability of $Ba_3Nb_{0.9}V_{0.1}MoO_{8.5}$ under reducing conditions is confirmed by thermogravimetric analysis coupled with mass spectroscopy performed in the temperature range 25 – 900 °C under dry air and 5% H_2 (in N_2), which shows the absence of any oxygen loss associated with reduction of the sample (Supporting Figure S13). The TGA-MS results clearly indicate that the detected weight loss is ascribable to loss of H_2O from the sample, in accordance with

the ability of $Ba_3NbMoO_{8.5}$ to uptake a significant amount of water at ambient conditions. [19, 39] X-ray diffraction demonstrates that there is no change in crystal structure (with no evidence of formation of secondary phases) after annealing of a sample under 5% H_2 (in N_2) at various temperatures, nor after the impedance spectroscopy measurements (Supporting Figure S14). In addition, the conductivity of $Ba_3Nb_{0.9}V_{0.1}MoO_{8.5}$ at 600 °C presents no sign of degradation after several days of measurement under dry air and 5% H_2 (in N_2) (Supporting Figure S15). These results reveal the excellent stability of $Ba_3Nb_{0.9}V_{0.1}MoO_{8.5}$ in the pO_2 range studied here. For comparison, Mg-doped $Na_{0.5}Bi_{0.5}TiO_3$ shows a significant loss in conductivity after 20 hours annealing at 600 °C under 5% H_2 (in N_2). [40] Longer ageing times (> 36 hours) leads to reduction of Bi^{3+} to metallic Bi and Ti^{4+} to Ti^{3+}, and to a significant *n*-type electronic component. [40] Similarly, heating of $La_2Mo_2O_9$ under reducing conditions results in the formation of parasitic phases with Mo in lower oxidation states and electronic conductivity. [41]

The Arrhenius plot in Figure 3 compares the bulk ionic conductivity of the x = 0.1 V-doped composition with the conductivity of other leading conductors. At ~ 600 °C the bulk conductivity of $Ba_3Nb_{0.9}V_{0.1}MoO_{8.5}$ (BNVM) is significantly higher than the conductivity of yttria stabilized zirconia ($Zr_{0.92}Y_{0.08}O_{1.96}$, YSZ), a state-of-the-art electrolyte which is commonly employed in commercially available SOFCs, [3] and of the oxygen ionic conductivity of $Ba_7Nb_4MoO_{20}$ (Ba7) measured in dry air. [39] The bulk conductivity is also comparable to the conductivities of $La_{0.8}Sr_{0.2}Ga_{0.83}Mg_{0.17}O_{2.815}$ (LSGM), [7] $La_2Mo_2O_9$ (LAMOX), [6] and Mg-doped $Na_{0.5}Bi_{0.5}TiO_3$ ($Na_{0.5}Bi_{0.49}Ti_{0.99}Mg_{0.01}O_{2.975}$, Mg-NBT). [8]

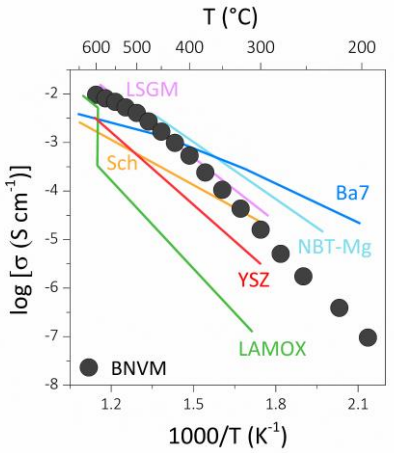

Figure 3. Comparison of the bulk conductivity of $Ba_3Nb_{0.9}V_{0.1}MoO_{8.5}$ (BNVM) with other leading ionic conductors; $Zr_{0.92}Y_{0.08}O_{1.96}$ (YSZ) (ref. 3), $La_{0.8}Sr_{0.2}Ga_{0.83}Mg_{0.17}O_{2.815}$ (LSGM) (ref. 7), $Na_{0.5}Bi_{0.49}Ti_{0.99}Mg_{0.01}O_{2.975}$ (NBT-Mg) (ref. 8), $La_2Mo_2O_9$ (LAMOX) (ref. 6), $Bi_{0.95}Sr_{0.05}VO_{3.975}$ (Sch) (ref. 14), and the bulk ionic conductivity in dry air of $Ba_7Nb_4MoO_{20}$ (ref. 39).

Rietveld refinement of the structural model from neutron and high-resolution laboratory X-ray diffraction data was employed to investigate the effect of V-substitution on the structural features of the $Ba_3Nb_{1-x}V_xMoO_{8.5}$ series. The average structure of $Ba_3NbMoO_{8.5}$ inferred from powder neutron diffraction has been described as a hybrid between the palmierite and 9R hexagonal perovskite. [16] In this model, the cation vacancies can be distributed on two partially occupied metal sites (M1 and M2), leading to the formation of hybrid trimer stacks of face-sharing polyhedral units in which two metal cations are disordered over three sites. However, a recent single crystal X-ray diffraction study has highlighted significant disorder in the cation sub-lattice. [18] There is large distortion of the central metal octahedron (M2) within the stack so that the original M2 3*b* Wyckoff position (0,0,0.5) is split into two mutually exclusive cation positions. Analysis of difference Fourier maps generated from the POLARIS neutron diffraction data by employing the average trimer stack model and setting the M2 occupancy to zero evidenced that the majority of the nuclear scattering density is located at (0,0,~0.52) (Wyckoff site 6*c*), above and below the nominal 3*b* position, analogously to what has been reported in the single crystal XRD study (Supporting Figure S16). A structural model with M2 on a split 6*c* position was therefore employed for the refinement of the powder neutron diffraction data (Supporting Table S2). Following previously published structural data, [16] the oxygen atoms were placed at three different Wyckoff positions: O1 at 18*h,* O2 at 9*e* and O3 at 36*i*; while barium atoms occupy the 6*c* and 3*a* sites (Ba1 and Ba2 respectively). The atomic displacement parameters, U, were modelled anisotropically for the Ba, M1, O1 and O2 atoms; isotropic displacement parameters, U_{iso}, were used for the split M2 and O3 positions. Ba and O1 fractional occupancies from neutron diffraction refined to within ±1% of full occupancy and were fixed at 1.0. The M1 and M2 fractional occupancies (g) were refined in the XRD model using a g(M1) = -g(M2) constraint, and then fixed in the refinement of the structure from neutron diffraction data. O2 and O3 fractional occupancies were refined from neutron diffraction giving the expected oxygen $O_{8.5}$ stoichiometry. The average structural model is shown in Figure 1c. An excellent Rietveld fit was obtained for all the compositions (Supporting Figure S17). The structural and statistical parameters obtained from the refinements are reported in Supporting Table S2. The symmetry $R\bar{3}m$ *H* is retained across the whole $Ba_3Nb_{1-x}V_xMoO_{8.5}$ (x = 0.0, 0.1, 0.2, 0.3, 0.4) series.

The M1 and M2 sites are partially occupied due to the short separation (~ 1.6 Å) between the two nearest metal positions, which makes the simultaneous occupation of these two sites unfavorable. Only two cation sites per hybrid stack can be occupied, leading to the formation on the local-scale of either two face-sharing polyhedral units (Figure 4a, configuration 1) or two separated polyhedral units spaced by a cation vacancy (Figure 4a, configuration 2) in agreement with results obtained from single crystal XRD. [18] The random distribution of the cation vacancies leads to the formation of complex disordered stacking configurations of the $M1O_x$ and $M2O_6$ polyhedral units (one possible configuration is shown in Figure 4b).

Supporting Figure S18 demonstrates that the fractional occupancy of M1 increases with x, while the fractional occupancy of M2 decreases. The V^{5+} cations are predominantly situated at the M1 site and the fractional occupancy of V^{5+} at this site increases with x. A small amount of V^{5+} substitutes for Nb^{5+} at the M2 positions although the concentration of V^{5+} on the M2 site plateaus for $x \geq 0.3$ (Supporting Figure S18b). The reduction in the overall M2 occupancy is further

driven by the rearrangement of Mo at the two metal sites as the concentration of V increases (Supporting Figure S18b). Figure 5a demonstrates that the fractional occupancy of O3 increases almost linearly with the vanadium concentration, while the fractional occupancy of O2 decreases. The relative occupation of the two average oxygen sites is associated with different MO_x polyhedral units. In the average structure, occupation of O3 leads to the formation of average $M1(O1_3O3)$ tetrahedral units, while occupation of O2 causes the formation of average $M1(O1_3O2_3)$ octahedral units (Figure 5b). On the local scale, the occurrence of neighboring tetrahedral and octahedral units, in conjunction with the large positional oxygen disorder, results in the formation of intermediate 5-fold geometries. [19] Due to the relative distances between the available oxygen sites, these 5-fold units are most likely constituted by distorted average $M1(O1_3O2O3)$ and $M1(O1_3O2_2)$ polyhedra (Figure 5b). The behavior of the O2/O3 fractional occupancies upon replacing Nb^{5+} by V^{5+} denotes an increase in the relative number of lower coordination polyhedral units.

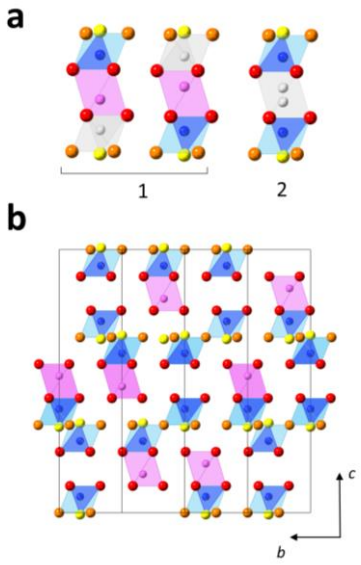

Figure 4. (a) Possible polyhedral stacks generated by partial occupation of the M1 and M2 positions. Grey polyhedra represent the empty cationic sites. (c) Schematic representation of a potential disordered arrangement of face-sharing and isolated stacking configurations of the MO_x and $M2O_6$ polyhedral units. O3 is represented at 6*c* for simplicity in all the figures.

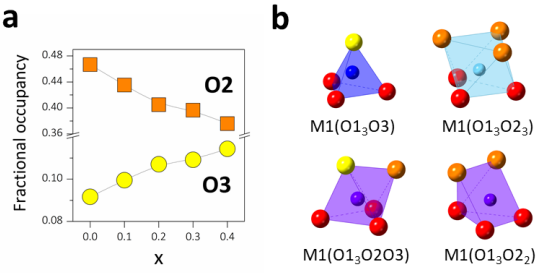

Figure 5. (a) Variation of the oxygen fractional occupancies of $Ba_3Nb_{1-x}V_xMoO_{8.5}$ upon increasing *x*. The fraction of O3 increases with V-doping, while O2 decreases. (b) Average MO_x polyhedral units formed by occupation of the O2 (orange) and O3 (yellow) crystallographic sites. O3 is represented at 6*c* for simplicity.

The decrease in O2 must lead to the reduction in the number of average 6-fold M1 units, while the increase in O3 can be associated with a general increase in the average $M1(O1_3O3)$ tetrahedral units. Due to its smaller ionic radius and high oxidation state, V^{5+} has a greater tendency to adopt lower coordination 4-fold environments than Nb^{5+}, [22] thus explaining the increase in O3 fractional occupancy with *x* in $Ba_3Nb_{1-x}V_xMoO_{8.5}$.

Bond-valence site energy (BVSE) calculations were employed to analyze the migration pathway and energy landscape of the oxide ion conduction in the average crystal structure of $Ba_3Nb_{1-x}V_xMoO_{8.5}$. Bond-valence based energy analysis has been extensively used for the investigation of conduction pathways in various oxide ion [10, 42, 43, 44, 45, 46, 47] and sodium and lithium ionic conductors. [48, 49, 50] The reliability of ionic conduction pathways obtained from bond-valence energy based methods has been confirmed by agreement with diffraction experiments and by results from maximum entropy studies and molecular dynamics calculations.[42, 47, 51, 52] Furthermore, BVS methods have been effective in the screening and successful discovery of novel oxide ion conductors. [42, 43, 44, 45] The low computational cost and reliability of the predicted relative migration energy barriers make *soft*BV particularly useful for further investigation of the conduction pathways of inherently complex disordered crystal phases such as $Ba_3Nb_{1-x}V_xMoO_{8.5}$, for which density functional theory (DFT) calculations might be particularly challenging and computationally expensive. [33] While it is expected that the detailed energy barriers will be determined by the local distribution of oxygen populations and metal stacking configurations, BVSE analysis on the average structure can provide useful general indications and trends on the energetics of ionic migration in $Ba_3Nb_{1-x}V_xMoO_{8.5}$, and as such can be used as proxy, in relative terms, for the activation energy determined by impedance spectroscopy measurements or more accurate computational DFT methods. [33, 47] BVSE calculations were performed with the *soft*BV program on all members of the $Ba_3Nb_{1-x}V_xMoO_{8.5}$ series. Bond-valence site energy landscapes for the interaction of a probe oxide ion were calculated from the refined structural models. A representative bond-valence energy map for $Ba_3Nb_{0.9}V_{0.1}MoO_{8.5}$ is presented in Figure 6. Two-dimensional O2-O3 conduction pathways (on the *ab* plane) corresponding with the lowest bond-valence site energy barriers are evidenced along the palmierite-like layers (Figure 6a), in accordance with a previous maximum entropy study. [20] This conduction pathway involves oxide ion diffusion through the partially occupied O2 and O3 oxygen sites over the O2-O2-O2 face of the MO_6 pseudo-octahedron, with facile reorganization of the coordination of the MO_x units. This migration mechanism differs from the one found in AMO_3 perovskites, where oxygen ions diffuse along a curved trajectory on the edge of the MO_6 octahedra. [20]

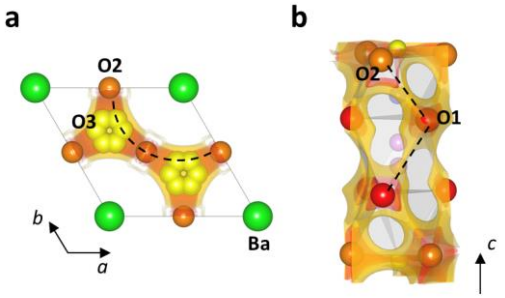

Figure 6. Bond-valence site energy map calculated for $Ba_3Nb_{0.9}V_{0.1}MoO_{8.5}$, as seen along the *c*-axis (a) and *b*-axis directions (b). Dashed lines highlight connectivity regions. Darker colors indicate the lower isosurface levels (< 0.4 eV over the global minimum), while the lighter colors are for the highest isosurface levels (> 0.7 eV over the global minimum).

Sizeable connectivity is also found between adjacent O1-O2 and O1-O1 positions (with saddle points at the median of the O1-O2 and O1-O1 distances) (Figure 6b), indicating oxygen motion within the fully occupied O1 sites. Similar connectivity has been observed in the bond-valence energy landscape maps obtained from single crystal X-ray diffraction data collected on $Ba_3NbMoO_{8.5}$. [18] Studies on $La_2Mo_2O_9$ (LAMOX) materials evidence that the oxide ions on the fully occupied apical oxygen sites of the MoO_x units can migrate, thus contributing to the ionic transport by intra-polyhedra diffusion towards the partially occupied equatorial oxygen sites. [53,54] It is hence possible to have a certain amount of O1 motion along the edges of the $M1O_x$ and $M2O1_6$ polyhedra also in $Ba_3Nb_{1-x}V_xMoO_{8.5}$, implying the presence of oxygen mobility parallel to the *c*-axis. However, the bond-valence energy landscape clearly shows that the 2-dimensional pathway along the disordered O2-O3 sites has a considerably lower relative bond-valence energy barrier (< 0.4 – 0.5 eV) than the O1-O2 and O1-O1 pathways (> 0.65 eV and > 1.1 eV respectively). Furthermore, the size of the bottleneck for oxygen diffusion on the *ab* plane is larger than the bottleneck for the *c*-axis. [20] Therefore, the pathway along the palmierite-like layer is most likely the dominant route contributing to the overall conduction. Molecular dynamics studies and single crystal conductivity measurements are required to confirm whether the oxygen transport in $Ba_3NbMoO_{8.5}$ materials is truly anisotropic, involving oxide ion migration exclusively along the palmierite-like layers.

Examination of the BVSE energy landscape obtained for the dominant 2-dimensional ionic conduction pathway along the palmierite-like layer reveals the presence of two saddle points with relative energy barriers. The saddle point *S*1 (with relative bond-valence energy barrier *E*1) corresponds to oxide ion exchange along the connected distribution of average oxygen sites O2/O3 (Figure 7a, bottom). Therefore, the relative energy term *E*1 is most likely influenced by the distribution of oxygen atoms on the average O2/O3 sites, which is associated with the dynamic mobility of the oxide ions. [18,21] *E*1 decreases with *x* (Supporting Figure S19), concomitantly with the increase in the occupation of the average tetrahedral position (Figure 5a). The increase in the O3 fractional occupancy leads to an increase in the number of lower coordination geometries, which is known to provide more favorable and dynamic environments for oxygen exchange between metal units, [12,13,14] thus explaining the reduction in *E*1 with vanadium concentration. The relationship between the height of *E*1 and the relative occupancy of O2/O3 is further corroborated by BVSE calculations on $Ba_3NbWO_{8.5}$. The relative *E*1 energy barrier for $Ba_3NbWO_{8.5}$, with ~12% of average O3 sites occupied at room temperature, [24] is substantially higher than for any of the members of the $Ba_3Nb_{1-x}V_xMoO_{8.5}$ series, where more than ~55% of O3 sites are occupied (Figure 7b). The second saddle point (*S*2) is perpendicular to the undulating distribution of crystallographic oxygen sites (Figure 7a, top). We associate its relative energy barrier (*E*2) with the average relaxation of the oxygen atoms induced by the coplanar alignment of the oxide ions during the exchange between O2 and O3. Migration along the *ab* plane requires a relaxation of the oxygen atoms in direction parallel to the *c*-axis of ~ 0.25 Å as a result of the undulating distribution of crystallographic sites. *E*2 is associated with the relaxation of the metal polyhedra during the oxygen exchange and therefore its height will be linked to the average distortion of the $M1O_x$ units. The latter can be evaluated by analysis of the minimum bonding ellipsoid, which is the ellipsoid of the smallest volume that encompasses all the atoms of a given coordination polyhedron. [36] Supporting Figure S20a shows that the distortion ($\sigma(R)$) of the average $M1O_x$ units increases with V-doping. In $Ba_3NbMoO_{8.5}$, the average metal polyhedra are distorted due to the out-of-center displacement resulting from the second-order Jahn-Teller distortion induced by the d^0 cations (Supporting Figure S20b). [16,18] The magnitude of this distortion is higher for cations with larger formal charge and smaller ionic radius. [55] Consequently, more distorted average coordination units are expected upon substitution of Nb^{5+} by V^{5+}, since the latter is a stronger distorter. [56] *E*2 increases along the $Ba_3Nb_{1-x}V_xMoO_{8.5}$ series (Supporting Figure S19), implying that the more distorted units have a higher relative energy barrier for the average relaxation involved in the oxygen migration exchange. In corroboration, $Ba_3NbWO_{8.5}$ does not present any *E*2 barrier due to the significantly smaller distortion of its $M1O_x$ units (0.047 Å) (Figure 7b).

The activation energy for the bulk conductivity obtained from the linear fit of the high temperature (T ≥ 500 °C) part of the Arrhenius plot presents a minimum at $x = 0.1$, corresponding with the maximum in the bulk conductivity value at 600 °C (Figure 7c). It is well-known that fluorite doped-ceria oxide ion conductors exhibit a similar trend, showing a maximum in conductivity accompanied with a minimum in activation energy at a certain dopant concentration. [57,58,59,60] In these systems, the increase in dopant fraction increases the number of carriers and leads to a decrease in the activation enthalpy due to favorable attractive coulombic interactions in the low-concentration regime. [57,58] However, above a certain dopant concentration threshold, (repulsive) interactions between vacancy-vacancy associates and dopant clusters leads to trapping of the oxygen vacancies, resulting in an increase in the activation enthalpy due to an unfavorable binding energy term. [58,59,60] Analogously, in the $Ba_3Nb_{1-x}V_xMoO_{8.5}$ series the behavior of the conductivity and activation energy can be ascribed to the contrasting influence of V-doping on the oxygen/vacancy distribution and the average polyhedral distortion. While the increase in O3 occupancy may generate more favorable coordination

environments for ionic conduction ($E1$ decreases), the increasing local distortion results in a higher energy barrier for the local relaxation/motion of the oxygen atoms ($E2$ increases) and acts as a trap for the mobile defects. [61]

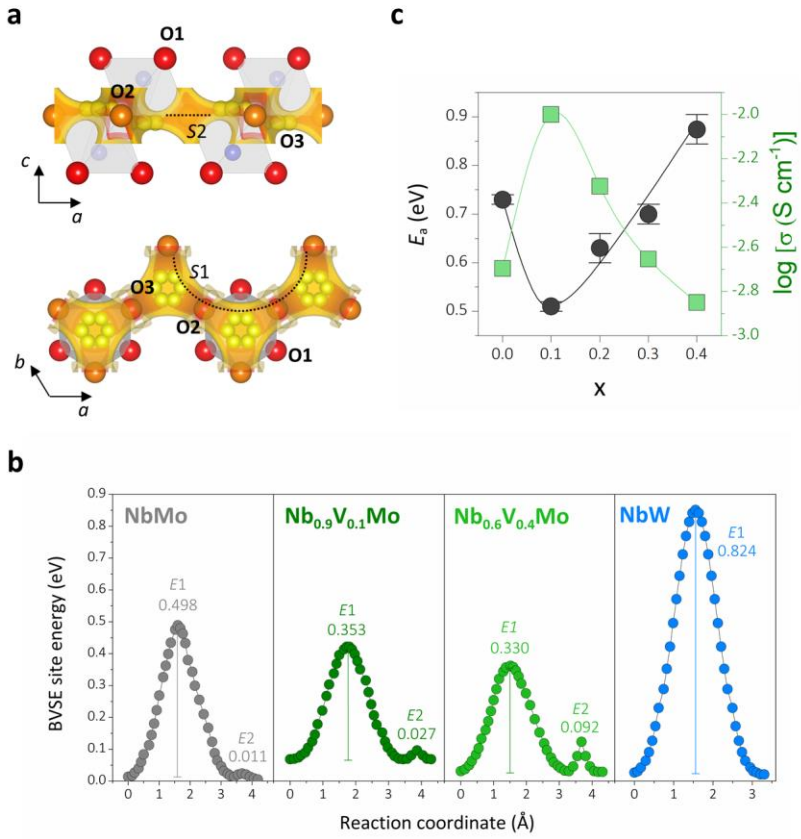

Figure 7. (a) BVSE map showing the 2-dimensional ionic conduction pathway along the palmierite-like layer as seen down the *c*-axis (bottom) and *b*-axis (top). The dotted lines represent the saddle points as identified by the *soft*BV software. (b) BVSE models of migration barriers along the palmierite-like layers for $Ba_3NbMoO_{8.5}$, $Ba_3Nb_{0.9}V_{0.1}MoO_{8.5}$, $Ba_3Nb_{0.6}V_{0.4}MoO_{8.5}$, and $Ba_3NbWO_{8.5}$. Bond-valence energy barriers are reported in eV. Note that the minimum site energies have relative values. (c) Bulk activation energy from the linear fit of the high temperature (T ≥ 500 °C) part of the Arrhenius plot and bulk conductivity values at 600 °C plotted against the amount of V doping *x*.

Conclusions

In summary, we have shown that the ionic conductivity of $Ba_3NbMoO_{8.5}$ can be significantly enhanced by substituting Nb^{5+} with V^{5+}. BVSE analysis on the $Ba_3Nb_{1-x}V_xMoO_{8.5}$ series demonstrates the presence of two relative energy barriers for the 2-dimensional oxygen diffusion along the palmierite-like layers. These barriers are relative to the populations of the average oxygen crystallographic sites ($E1$) and to the average distortion of the flexible $M1O_x$ units ($E2$). V-doping leads to an increase in the fractional occupancy of the average tetrahedral position O3, and to a reduction in the relative energy term $E1$ associated with the oxide ion exchange along the connected distribution of crystallographic oxygen sites. On the other hand, the increasing local distortion induced by V-doping increases the relative height of the $E2$ energy barrier. This antagonistic behavior results in a minimum in the bulk activation energy for the sample with x = 0.1. $Ba_3Nb_{0.9}V_{0.1}MoO_{8.5}$ exhibits the highest ionic conductivity among the doped series, due to a trade-off between an optimum distribution of local coordination geometries in the palmierite-like layers and the degree of distortion of the $M1O_x$ polyhedral units, the latter most likely acting as a trap for the mobile oxygen defects. The oxide ion diffusion mechanism will also depend on the local arrangement of the cationic species and on the local distribution of cation vacancies and coordination environments. As such further analysis by local probes (e.g. pair distribution function analysis, solid-state NMR) and computational DFT studies are warranted. The results described here, based on BVSE analysis of the average description of the crystal structure, provide a first general insight into the energetics of ionic migration in these systems, and are valuable for further computational studies and for potentially improving the conductivity of $Ba_3NbMoO_{8.5}$-based compounds even further. Finally, the high bulk ionic conductivity (~ 0.01 S cm^{-1} at 600 °C) and stability of $Ba_3Nb_{0.9}V_{0.1}MoO_{8.5}$ make this material suitable for possible practical applications, with also the potential of further enhancing its electrical and physicochemical properties by fine doping around x = 0.1 and/or co-doping.

ASSOCIATED CONTENT

Supporting Information. The supporting information includes figures and tables of crystallographic data, figures showing electrical data, SEM micrographs and thermogravimetric data.

AUTHOR INFORMATION

Corresponding Authors

* **Sacha Fop** - Department of Chemistry, University of Aberdeen, Aberdeen AB24 3UE, United Kingdom; orcid.org/0000-0003-4168-6363; Email: sacha.fop1@abdn.ac.uk

* **Abbie C. Mclaughlin** - Department of Chemistry, University of Aberdeen, Aberdeen AB24 3UE, United Kingdom; /orcid.org/0000-0001-9960-723X Email: a.c.mclaughlin@abdn.ac.uk

Author Contributions

S.F. and K.S.M. synthesized and characterized the as prepared materials. S.F. performed the electrical characterization and analyzed the data with guidance from A.C.M. The structural characterization was performed by S.F. with contribution from K.S.M. and guidance from A.C.M. and R.I.S. S.F. performed the BVSE calculations and distortion analysis. S.F. and A.C.M. wrote the manuscript. A.C.M. designed the study and directed the project.

Funding Sources

This research was supported by the Leverhulme trust and the University of Aberdeen.

Notes

The authors declare no competing financial interest.

ACKNOWLEDGMENT

We also acknowledge STFC-GB for provision of beamtime at ISIS.

REFERENCES

(1) Wachsman, E. D.; Lee, K. T. Lowering the Temperature of Solid Oxide Fuel Cells. *Science* **2011**, *334*, 935-939.

(2) Laguna-Bercero, M. A. Recent Advances in High Temperature Electrolysis Using Solid Oxide Fuel Cells: a Review. *Journal of Power Sources* **2012**, *203*, 4-16.

(3) Jacobson, A. J. Materials for Solid Oxide Fuel Cells. *Chem. Mater*. **2000**, *22*, 660-674.

(4) Inaba, H.; Tagawa, H. Ceria-based Solid Electrolytes. *Solid State Ionics* **1996**, *83*, 1-16.

(5) Abraham, F.; Boivin, J. C.; Mairesse, G.; Nowogrocki, G. The BIMEVOX Series: A New Family of High Performances Oxide Ion Conductors. *Solid State Ionics* **1990**, *40-41*, 934-937.

(6) Lacorre, P.; Goutenoire, F.; Bohnke, O.; Retoux, R.; Laligant, Y. Designing Fast Oxide-Ion Conductors Based on $La_2Mo_2O_9$. *Nature* **2000**, *404*, 856-858.

(7) Huang, K.; Tichy, R. S.; Goodenough, J. B. Superior Perovskite Oxide-Ion Conductor; Strontium- and Magnesium-Doped $LaGaO_3$: I, Phase Relationships and Electrical Properties. *J Am Ceram Soc* **1998**, *81*, 2565-2575.

(8) Li, M.; Pietrowski, M. J.; De Souza, R. A.; Zhang, H.; Reaney, I. M.; Cook, S. N.; Kilner, J. A.; Sinclair, D. C. A Family of Oxide Ion Conductors Based on the Ferroelectric Perovskite $Na_{0.5}Bi_{0.5}TiO_3$. *Nat. Mater.* **2013**, *13*, 31-35.

(9) Goodenough, J. B.; Ruiz-Diaz, J. E.; Zhen, Y. S. Oxide-ion Conduction in $Ba_2In_2O_5$ and $Ba_3In_2MO_8$ (M=Ce, Hf, or Zr). *Solid State Ionics* **1990**, *44*, 21-31.

(10) Fujii, K.; Esaki, Y.; Omoto, K.; Yashima, M.; Hoshikawa, A.; Ishigaki, T.; Hester, J. R. New Perovskite-Related Structure Family of Oxide-Ion Conducting Materials $NdBaInO_4$. *Chem. Mater.* **2014**, *26*, 2488-2491.

(11) Kendrick, E.; Islam, M. S.; Slater, P. R. Developing Apatites for Solid Oxide Fuel Cells: Insight into Structural, Transport and Doping Properties. *J. Mater. Chem.* **2007**, *17*, 3104-3111.

(12) Kendrick, E.; Kendrick, J.; Knight, K. S.; Islam, M. S.; Slater, P. R. Cooperative Mechanisms of Fast-Ion Conduction in Gallium-Based Oxides with Tetrahedral Moieties. *Nat. Mater.* **2007**, *6*, 871-875.

(13) Kuang, X.; Green, M. A.; Niu, H.; Zajdel, P.; Dickinson, C.; Claridge, J. B.; Jantsky, L.; Rosseinsky, M. J. Interstitial Oxide Ion Conductivity in the Layered Tetrahedral Network Melilite Structure. *Nat. Mater.* **2008**, *7*, 498-504.

(14) Yang, X.; Fernández-Carrión, A. J.; Wang, J.; Porcher, F.; Fayon, F.; Allix, M.; Kuang, X. Cooperative Mechanisms of Oxygen Vacancy Stabilization and Migration in the Isolated Tetrahedral Anion Scheelite Structure. *Nat. Commun.* **2018**, *9*, 4484.

(15) Peet, J. R.; Fuller, C. A.; Frick, B.; Zbiri, M.; Piovano, A.; Johnson, M. R.; Evans, I. R. Direct Observation of Oxide Ion Dynamics in $La_2Mo_2O_9$ on the Nanosecond Timescale. *Chem. Mater.* **2017**, *29*, 3020-3028.

(16) Fop, S.; Skakle, J. M. S.; McLaughlin, A. C.; Connor, P. A.; Irvine, J. T. S.; Smith, R. I.; Wildman, E. J. Oxide Ion Conductivity in the Hexagonal Perovskite Derivative $Ba_3MoNbO_{8.5}$. *J. Am. Chem. Soc.* **2016**, *138*, 16764-16769.

(17) Darriet, J.; Subramanian, M. A. Structural relationships between compounds based on the stacking of mixed layers related to hexagonal perovskite-type structures. *J. Mater. Chem.* **1995**, *5*, 543-552.

(18) Auckett, J. E.; Milton, K. L.; Evans, I. R. Cation Distributions and Anion Disorder in $Ba_3NbMO_{8.5}$ (M = Mo, W) Materials: Implications for Oxide Ion Conductivity. *Chem. Mater.* **2019**, *31*, 1715-1719.

(19) Chambers, M. S.; McCombie, K. S.; Auckett, J. E.; McLaughlin, A. C.; Irvine, J. T. S.; Chater, P. A.; Evans, J. S. O.; Evans, I. R. Hexagonal Perovskite Related Oxide Ion Conductor $Ba_3NbMoO_{8.5}$: Phase Transition, Temperature Evolution of the Local Structure and Properties. *J. Mater. Chem. A* **2019**, *7*, 25503-25510.

(20) Yashima, M.; Tsujiguchi, T.; Fujii, K.; Niwa, E.; Nishioka, S.; Hester, J. R.; Maeda, K. Direct Evidence for Two-Dimensional Oxide-Ion Diffusion in the Hexagonal Perovskite-Related Oxide $Ba_3MoNbO_{8.5-\delta}$. *J. Mater. Chem. A* **2019**, *7*, 13910-13916.

(21) Fop, S.; Wildman, E. J.; Irvine, J. T. S.; Connor, P. A.; Skakle, J. M. S.; Ritter, C.; Mclaughlin, A. C. Investigation of the Relationship Between the Structure and Conductivity of the Novel Oxide Ionic Conductor $Ba_3MoNbO_{8.5}$. *Chem. Mater.* **2017**, *29*, 4146-4152.

(22) Waroquiers, D.; Gonze, X.; Rignanese, G.; Welker-Nieuwoudt, C.; Rosowski, F.; Göbel, M.; Schenk, S.; Degelmann, P.; André, R.; Glaum, R.; Hautier, G. Statistical Analysis of Coordination Environments in Oxides. *Chem. Mater.* **2017**, *29*, 8346-8360.

(23) Fop, S.; Wildman, E. J.; Skakle, J. M. S.; Ritter, C.; Mclaughlin, A. C. Electrical and Structural Characterization of $Ba_3Mo_{1-x}Nb_{1+x}O_{8.5-x/2}$: The Relationship between Mixed Coordination, Polyhedral

Distortion and the Ionic Conductivity of $Ba_3MoNbO_{8.5}$. *Inorg. Chem.* **2017**, *56*, 10505-10512.

(24) McCombie, K. S.; Wildman, E. J.; Fop, S.; Smith, R. I.; Skakle, J. M. S.; Mclaughlin, A. C. The Crystal Structure and Electrical Properties of the Oxide Ion Conductor $Ba_3WNbO_{8.5}$. *J. Mater. Chem. A* **2018**, *6*, 5290-5295.

(25) McCombie, K. S.; Wildman, E. J.; Ritter, C.; Smith, R. I.; Skakle, J. M. S.; Mclaughlin, A. C. Relationship between the Crystal Structure and Electrical Properties of Oxide Ion Conducting $Ba_3W_{1.2}Nb_{0.8}O_{8.6}$. *Inorg. Chem.* **2018**, *57*, 11942-11947.

(26) Bernasconi, A.; Tealdi, C.; Mühlbauer, M.; Malavasi, L. Synthesis, Crystal Structure and Ionic Conductivity of the $Ba_3Mo_{1-x}W_xNbO_{8.5}$ solid solution. *Journal of Solid State Chemistry* **2018**, *258*, 628-633.

(27) Bernasconi, A.; Tealdi, C.; Malavasi, L. High-Temperature Structural Evolution in the $Ba_3Mo_{(1-x)}W_xNbO_{8.5}$ System and Correlation with Ionic Transport Properties. *Inorg. Chem.* **2018**, *57*, 6746-6752.

(28) Fop, S.; McCombie, K. S.; Wildman, E. J.; Skakle, J. M. S.; Mclaughlin, A. C. Hexagonal Perovskite Derivatives: a New Direction in the Design of Oxide Ion Conducting Materials. *Chem. Commun.* **2019**, *55*, 2127-2137.

(29) Boukamp, B. A. A Linear Kronig-Kramers Transform Test for Immittance Data Validation. *Journal of The Electrochemical Society* **1995**, *142*, 1885-1894.

(30) Schönleber, M., Klotz, D. & Ivers-Tiffée, E. A Method for Improving the Robustness of Linear Kramers-Kronig Validity tests. *Electrochimica Acta* **2014**, *131*, 20-27.

(31) Toby, B. H. EXPGUI, a Graphical User Interface for GSAS. *Journal of Applied Crystallography* **2001**, *34*, 210-213.

(32) Sears, V. F. Neutron Scattering Lengths and Cross Sections. *Neutron News* 1992, **3**, 29-37.

(33) Chen, H.; Wong, L. L.; Adams, S. *Soft*BV: a Software Tool for Screening the Materials Genome of Inorganic Fast Ion Conductors. *Acta Crystallographica Section B* **2019**, *75*, 18-33.

(34) Chen, H.; Adams, S. Bond Softness Sensitive Bond-Valence Parameters for Crystal Structure Plausibility Tests. *IUCrJ* **2017**, *4*, 614-625.

(35) Adams, S. Relationship Between Bond Valence and Bond Softness of Alkali Halides and Chalcogenides. *Acta Crystallographica Section B* **2001**,57, 278-287.

(36) Cumby, J.; Attfield, P. Ellipsoidal Analysis of Coordination Polyhedra. Nat. Commun. **2017**, *8*, 14235.

(37) Irvine, J. T. S.; Sinclair, D. C.; West, A. R. Electroceramics: Characterization by Impedance Spectroscopy. *Adv. Mater.* **1990**, *2*, 132-138.

(38) Verbraeken, M. C., Cheung, C., Suard, E. & Irvine, J. T. S. High H- Ionic Conductivity in Barium Hydride. *Nat. Mater.* **14**, 95-100 (2014).

(39) Fop, S.; McCombie, K. S.; Wildman, E. J.; Skakle, J. M. S.; Irvine, J. T. S.; Connor, P. A.; Savaniu, C.; Ritter, C.; Mclaughlin, A. C. High Oxide Ion and Proton Conductivity in a Disordered Hexagonal Perovskite. *Nat. Mater.* **2020**, https://doi.org/10.1038/s41563-020-0629-4.

(40) Bhattacharyya, R.; Das, S.; Omar, S. Long-term conductivity stability of acceptor-doped $Na_{0.54}Bi_{0.46}TiO_{3-\delta}$. *Solid State Ionics* **2019**, *330*, 40-46.

(41) Marrero-López, D.; Canales-Vázquez, J.; Ruiz-Morales, J. C.; Irvine, J. T. S.; Núñez, P. Electrical conductivity and redox stability of $La_2Mo_{2-x}W_xO_9$ materials. *Electrochimica Acta* **2005**, *50*, 4385-4395.

(42) Zhang, W.; Fujii, K.; Niwa, E; Hagihala, M.; Kamiyama, T.; Yashima, M. Oxide-ion conduction in the Dion–Jacobson phase $CsBi_2Ti_2NbO_{10-\delta}$. *Nat. Commun.* **2020**, *11*, 1224.

(43) Yasui, Y.; Niwa, E.; Matsui, M.; Fujii, K.; Yashima, M. Discovery of a Rare-Earth-Free Oxide-Ion Conductor $Ca_3Ga_4O_9$ by Screening through Bond Valence-Based Energy Calculations, Synthesis, and Characterization of Structural and Transport Properties. *Inorg. Chem.* **2019**, *58*, 9460-9468.

(44) Niwa, E.; Yashima, M. Discovery of Oxide-Ion Conductors with a New Crystal Structure, $BaSc_{2-x}A_xSi_3O_{10-x/2}$ (A = Mg, Ca) by Screening Sc-Containing Oxides through the Bond-Valence Method and Experiments. *ACS Appl. Energy Mater.* **2018**, *1*, 4009-4015.

(45) Inoue, R.; Fujii, K.; Shiraiwa, M.; Niwa, E.; Yashima, M. A new structure family of oxide-ion conductors $Ca_{0.8}Y_{2.4}Sn_{0.8}O_6$ discovered by a combined technique of the bond-valence method and experiments. *Dalton Trans.* **2018**, *47*, 7515-7521.

(46) Fujimoto, A.; Yashima, M.; Fujii, K.; Hester, J. R. New Oxide-Ion Conductor SrYbInO4 with Partially Cation-Disordered $CaFe_2O_4$-Type Structure. *J. Phys. Chem. C* **2017**, *121*, 21272-21280.

(47) Tate, M. L.; Fuller, C. A.; Avdeev, M.; Brand, H. E. A.; McIntyre, G. J.; Radosavljevic Evans, I. Synthesis and Characterisation of New Bi(iii)-containing Apatite-type Oxide Ion Conductors: the Influence of lone Pairs. *Dalton Trans.* **2017**, *46*, 12494-12499.

(48) Duchardt, M.; Neuberger, S.; Ruschewitz, U.; Krauskopf, T.; Zeier, W. G.; Schmedt auf der Günne, Jörn; Adams, S.; Roling, B.; Dehnen, S. Superion Conductor $Na_{11.1}Sn_{2.1}P_{0.9}Se_{12}$: Lowering the Activation Barrier of Na^+ Conduction in Quaternary 1-4-5-6 Electrolytes. *Chem. Mater.* **2018**, *30*, 4134-4139.

(49) Zhou, L.; Assoud, A.; Shyamsunder, A.; Huq, A.; Zhang, Q.; Hartmann, P.; Kulisch, J.; Nazar, L. F. An Entropically Stabilized Fast-Ion Conductor: $Li_{3.25}[Si_{0.25}P_{0.75}]S_4$. *Chem. Mater.* **2019**, *31*, 7801-7811.

(50) Park, K.; Kaup, K.; Assoud, A.; Zhang, Q.; Wu, X.; Nazar, L. F. High-Voltage Superionic Halide Solid Electrolytes for All-Solid-State Li-Ion Batteries. *ACS Energy Lett.* **2020**, *5*, 533-539.

(51) Uno, W.; Fujii, K.; Niwa, E.; Torii, S.; Miao, P.; Kamiyama, T.; Yashima, M. Experimental visualization of oxide-ion diffusion paths in pyrochlore-type $Yb_2Ti_2O_7$. *Journal of the Ceramic Society of Japan* **2018**, *126*, 341-345.

(52) Yang, X.; Liu, S.; Lu, F.; Xu, J.; Kuang, X. Acceptor Doping and Oxygen Vacancy Migration in Layered Perovskite $NdBaInO_4$-Based Mixed Conductors. *J. Phys. Chem. C* **2016**, *120*, 6416-6426.

(53) Corbel, G.; Suard, E.; Lacorre, P. Structural Key of the Thermal Expansion and the Oxide Ionic Conduction in Derivatives of $La_2Mo_2O_9$: a Temperature-Controlled Neutron Diffraction Study of β-$La_{1.7}Bi_{0.3}Mo_2O_9$. *Chem. Mater.* **2011**, *23*, 1288-1298.

(54) Peet, J. R.; Fuller, C. A.; Frick, B.; Zbiri, M.; Piovano, A.; Johnson, M. R.; Evans, I. R. Direct Observation of Oxide Ion Dynamics in $La_2Mo_2O_9$ on the Nanosecond Timescale. *Chem. Mater.* **2017**, *29*, 3020-3028.

(55) Kunz, M.; Brown, I. D. Out-of-Center Distortions around Octahedrally Coordinated d^0 Transition Metals. *J. Solid State Chem.* **1995**, *115*, 395– 406.

(56) Ok, K. M.; Halasyamani, P. S.; Casanova, D.; Llunell, M.; Alemany, P.; Alvarez, S. Distortions in Octahedrally Coordinated d^0 Transition Metal Oxides: A Continuous Symmetry Measures Approach. *Chem. Mater.* **2006**, *18*, 3176-3183.

(57) Faber, J.; Geoffroy, C.; Roux, A.; Sylvestre, A.; Abélard, P. A Systematic investigation of the dc electrical conductivity of rare-earth doped ceria. *Applied Physics A* **1989**, *49*, 225-232.

(58) Wang, D. Y.; Park, D. S.; Griffith, J.; Nowick, A. S. Oxygen-ion conductivity and defect interactions in yttria-doped ceria. *Solid State Ionics* **1981**, *2*, 95-105.

(59) Buyukkilic, S.; Kim, S.; Navrotsky, A. Defect Chemistry of Singly and Doubly Doped Ceria: Correlation between Ion Transport and Energetics. *Angew. Chem. Int. Ed.* **2014**, *53*, 9517-9521.

(60) Koettgen, J.; Grieshammer, S.; Hein, P.; Grope, B. O. H.; Nakayama, M.; Martin, M. Understanding the ionic conductivity maximum in doped ceria: trapping and blocking. *Phys. Chem. Chem. Phys.* **2018**, *20*, 14291-14321.

(61) Ding, J.; Balachandran, J.; Sang, X.; Guo, W.; Anchell, J. S.; Veith, G. M.; Bridges, C. A.; Cheng, Y.; Rouleau, C. M.; Poplawsky, J. D.; Bassiri-Gharb, N.; Unocic, R. R.; Ganesh, P. The Influence of Local Distortions on Proton Mobility in Acceptor Doped Perovskites. *Chem. Mater.* **2018**, *30*, 4919-4925.

Insert Table of Contents artwork here